A GEOCHEMISTRY BASED SCENARIO FOR TECTONIC SETTING OF MAFIC BODIES IN SOUTHERN QORVEH, WESTERN IRAN

Mohsen Karami Hatamabadi[1, 1], Seyed Jamal Sheikhzakariaee[1, *2], Mohammadhashem Emami[1, 3], Mehran Arian[1, 4]

Abstract

In the central part of the Sanandaj-Sirjan zone (C-SaSZ) in southern Ghorveh, western Iran two different types of gabbroic rocks in terms of mineralogical characteristics and chemical composition of the same age (late Jurassic) exists in the vicinity of each other including the olivine-bearing gabbroic rocks (OGRs) and the amphibole-bearing gabbroic rocks (AGRs). The effective process in magma's evolution of OGRs is differentiation. In the second category, digestion and/or mixing also occurred in addition to differentiation due to the geochemical positive anomalies of Pb, Rb, Ba, Th, and U. The AGRs have a high content of LIL elements and a low content of HFSEs. In particular, they have low Nb, Ti, and Ta contents. Zr depletion and low Zr/Sm and Zr/Ti ratios in these rocks indicate that their magma formed at a shallow depth (upper parts of the mantle). The melting of the mantle at a shallow depth, which produced the magma of the AGRs as a result of the fluids released from a sub ducting slab (subduction of the Neo-Tethys Ocean under the Iranian Plateau), is a step in the development of OGRs. Ascending magma has created a rift, which has caused the pressure on the underlying rocks to decrease at a steady temperature, melting the mantle. This mechanism leads to the creation of OGRs.

Keywords: Continental rift, depleted mantle, enriched mantle, magma mixing, Sanandaj Sirjan zone.

[1]Department of Geology, Faculty of Converging Technologies, Islamic Azad University, Science and Research Branch, Tehran, Iran

[1]Mohsen Karami Hatamabadi: m.karami@srbiau.ac.ir, Graduate student (doctor course)

[3] Mohammadhashem Emami: emami@srbiau.ac.ir, Professor

[4] Mehran Arian: Mehran Arian@srbiau.ac.ir, Professor

[2] ***Corresponding author:**
Seyed Jamal Sheikhzakariaee
Email: Sheikhzakariaee@srbiau.ac.ir, Researcher, Tel: +98 910-247-1346

DOI: 10.53555/ecb/2022.11.12.213

.1. INTRODUCTION

Gabbroic rocks in a region usually have similar characteristics, but in the south of Qorveh (western Iran), gabbroic rocks of the same age have different characteristics in terms of color, mineralogy, and other lithological characteristics.

The gabbroic rocks of this area can be divided into two general categories, first, olivine-bearing gabbroic rocks (OGRs) with a lighter color, and second, amphibole-bearing gabbroic rocks (AGRs) with a darker color (Ghalamghash et al., 2018; Azizi and Stern, 2019; Azizi et al., 2020).

Several origins have been proposed for the gabbro rocks worldwide, such as enriched mantle (Willbold et al., 2010), depleted mantle (Salters, 2004), and fractionation of ultramafic complexes (McCallum, 1996; Cawthorn et al., 1998; Mungall et al., 2016). Based on the size of the gabbroic bodies, only the first and second origins can be considered probable for them. According to the age measurements, these gabbroic rocks and the adjacent acidic rocks are almost in the same age range (late Jurassic) (Ghalamghash et al., 2018; Azizi and Stern, 2019; Azizi et al., 2020;).

The gabbroic bodies are located in the central part of the Sanandaj-Sirjan zone (SaSZ). This zone is located between the Zagros zone in the west and the Urmiah Dokhtar magmatic arc (UDMA) in the east and is known for numerous intrusions and metamorphisms caused by the subduction of the Tethys and Neo-Tethys oceans under the Iranian plateau (Nabavi, 1976; Bird, 1978; Alavi, 1980; Berberian et al., 1981; Sengor, 1990; Alavi, 1994; Berberian, 1995; Bushara, 1995; Sabzai et al., 1997; Babaie et al., 2000; Mohajjel et al., 2000; Agard et al., 2005; Agard et al., 2011; Verdel et al., 2011); and contains a wide range of intrusive bodies and metamorphic rocks (Ahadnejad et al., 2011; Mahmoudi et al., 2011; Azizi et al., 2013; Azizi et al., 2015; Deevsalar et al., 2017; Deevsalar et al., 2018; Mahmoudi et al., 2019).

These gabbroic bodies are not far from each other (a few kilometers away), and their names are usually similar to those of the nearest village (Ahadnejad et al., 2011; Mahmoudi et al., 2011; Azizi et al., 2013; Azizi et al., 2015; Deevsalar et al., 2017; Deevsalar et al., 2018; Mahmoudi et al., 2019).

We clarify the geodynamics and tectonic setting of late Jurassic gabbroic rocks in the central part of C-SaSZ in this study and based on our findings and the findings of previous studies, we propose a scenario about the evolution of mafic magma and the formation of gabbro bodies in southern Ghorveh.

2. GEOLOGICAL SETTING AND FIELD OBSERVATIONS

The Iranian Plateau is a part of the Alpine-Himalayan orogenic belt and is mainly formed by joining several sub-continents separated by deep faults. The sub-continents are connected by the closure of the Tethys Ocean (Stöcklin et al., 1973; Alavi, 1994; Saki, 1994; Agard et al., 2005; Allen et al., 2008; Ghalamghash et al., 2009; Mazhari et al., 2009; Agard et al., 2011; Ballato et al., 2011; Chiu et al., 2013; Mohammadi et al., 2013; Lehmann et al., 2018; Azizi et al., 2019a, 2019b).

Between the Zagros and UDMA structural zones, which are in the west and east, respectively, is where the SaSZ is situated (Fig. 1). In the SaSZ, intrusive bodies are highly common, and this zone is typically renowned for having a large number of intrusive bodies (Ahmadi-Khalaji et al., 2007; Ahadnejad et al., 2011; Alirezaei et al., 2012; Esna-Ashari et al., 2012; Sabeti et al., 2012; Azizi et al., 2015; Bayati et al., 2017; Shabanian et al., 2020; Shakerardakani et al., 2020). Most of the intrusive bodies were injected in four main stages, each stage is associated with an important tectonic event.

Figure 1 is about here

The first stage is related to 650–450 million years ago, happened in the central and northern parts of the SaSZ, and was related to the subduction of Proto-Tethys under Gondwana. The rocks left over from this period are known as the bedrock of Cadomian in the north and northwest of Iran (Shafaii Moghadam et al., 2017; Daneshvar et al., 2019; Moradi et al., 2020;).

The second stage is mainly related to 350-330 million years ago and is often seen in the northern parts of SaSZ (Moghadam et al., 2015; Abdulzahra et al., 2016; Azizi et al., 2017; Mohammadi et al., 2019).

The Jurassic period was the site of the third stage of magma intrusion (early Cretaceous is also mentioned in some cases). These plutons are mostly seen in the central part of SaSZ (Azizi and Stern, 2019).

The fourth part of the intrusive bodies is mostly seen in the northern part of SaSZ and its age is estimated to be 55 to 40 million years ago (Bea et al., 2011; Mazhari et al., 2011; Sepahi et al., 2014; Azizi et al., 2019a, 2019b).

The gabbroic bodies of southern Qorveh are from the third phase and cut the Jurassic metamorphic complex in the region (Fig. 2).

The outcropping rock units in the region mainly include magmatic (gabbro and, to a lesser amount granite, diorite, and syenite) and metamorphic (regional, thermal, and dynamic) rocks (Fig. 2).

The following is the procedure for placing bodies made of gabbro, diorite, syenite, and granite: Magma that was gabbroic and dioritic initially penetrated. Although granitic magma has been replaced in the subsequent stage, acidic and mafic magmatism in the area can be thought of virtually concurrently based on the evidence of mixing, mingling, and syn-plutonic brecciated mafic dykes in the area. In the final phase of magmatic processes, syenitic magma has entered (Ghalamghash et al., 2018).

Gabbroic bodies have formed some low hills in the vicinity of Galali village (Fig. 3a–d), but in other areas, they are seen in mountainous parts.

The gabbroic rocks are invaded by white color granites. In some parts (areas around the villages

of Zarineh, Meihem, etc.) Magma mixing and mingling can be seen in the interference zone (Mollaei et al., 2017).

Figure 2 is about here

3. PETROGRAPHY

The gabbroic samples from the Galali intrusive body have a granular texture and were mainly composed of pyroxene and plagioclase from labradorite to anorthite (Fig. 4a–p) (Petrographic data of other gabbroic rocks in the region are reported by Mollaei et al., 2017 and Azizi et al., 2020).

Figure 3 is about here

Pyroxenes have an average size of 1.1 mm and can be automorphic to amorphous (in certain cases with twining) (Fig. 4c–p). The pyroxenes are augite based on their optical characteristics. While ophitic textures are occasionally seen, single crystals of these minerals are frequently seen too. Pyroxenes are altered to become amphibole, biotite, allanite, chlorite, and opaque minerals.

The pyroxenes are frequently transformed into biotite, opaque minerals, and chlorite in the middle, and allanite and amphibole at the rims. Amphibole and opaque minerals have totally replaced some pyroxenes (Fig. 4e–p).

Plagioclases are found in the form of auto-morph to amorphous with different sizes (medium to coarse crystal) and in some cases with albite-pericline twins, Carlsbad twins, and normal zoning (Fig. 4a–l). Based on optical properties and refractive index, plagioclases in samples range from labradorite to anorthite. Some of the plagioclases have been altered; the alteration products of these plagioclases include sericite and rarely calcite. In plagioclases with normal zoning, alteration to sericite can be seen in their central parts (Fig. 4i–j).

Figure 4 is about here

4. ANALYTICAL TECHNIQUE

After conducting petrographic studies, 29 samples were selected for chemical analysis. Major oxides were measured by X-ray fluorescence analysis using a Philips PW1480 spectrometer at Binaloud Mines Company (Iran). Concentrations of trace elements, including rare earth elements (REEs), were obtained using an inductively coupled plasma mass spectrometer (ICP-MS, PERKIN ELMER ELAN9000) at Binaloud Mines Company, too.

5. WHOLE ROCK GEOCHEMISTRY AND ELEMENTS PATTERN

The data obtained from XRF (10 samples) and ICP_MS (29 samples) analyses from the Galali intrusive body are presented in Table 1 (Geochemical data of other gabbroic rocks in the region are reported by Mollaei Yeganeh et al., 2017 and Azizi et al., 2020).

The TAS diagram (Cox et al., 1979) was used for rock chemical classification. This diagram shows all samples in the gabbro field and subalkaline/tholeiitic section (Fig. 5).

Harker diagrams illustrate a decrease in TiO_2, MgO, $Fe2O3^t$, CaO, and K_2O; an increase in Na_2O for the major oxides; and a decrease in the transitional elements (e.g., Ni, Cr, and Co) with increasing SiO_2 content (wt.%) (Fig. 6a–i).

La, Ho, and Yb were selected as representatives of LREE, MREE, and HREE, respectively. The Harker diagram for La shows a positive trend, while Ho and Yb, show a flat and negative trend, respectively (Fig. 6j–l).

Figure 5 is about here

The samples have a minimum amount of mg-number [MgO/ (MgO+FeOt) × 100]. The average magnesium number of the samples is 42.67, the lowest number is 40.83 and the highest number is 44.4. The samples also have low Nb (2.1 to 3.2 ppm) contents.

To better understand magma formation and evolution processes, normalized spider diagrams with chondrite (Thompson, 1982), primitive mantle (McDonough and Sun, 1995), MORB (Pearce, 1983), and lower crust (Weaver and Tarney, 1984) were used (Fig. 7a–d).

Table 1 is about here

Figure 6 is about here

All incompatible trace elements are enriched compared to the primitive mantle and chondrite, and LIL elements are more enriched than HFSEs (Fig. 7a–b). For example, the concentration of La changes between 20 to 30 times compared to the

chondrite. The rare earth elements normalized to the chondrite define two different patterns. Light REEs have an almost flat trend, whereas HREEs show a concave downward trend. A positive anomaly of Eu can be seen in the samples due to the presence of amphibole in the samples (Claeson et al., 2004) (Fig. 7b).

Normalized diagrams with MORB show the depletion of some elements and the enrichment of others. Strong enrichment of U, Rb, and Th elements, positive anomalies of Sr, K, Pb, Ba, Ta, P, La, Ce, Hf, and Sm, and negative anomalies of Ti, Zr, Y, Yb, elements are common among samples (Fig. 7c).

Rb, Th, and U elements are enriched in the normalized diagram of the lower crust, whereas Ba and Zr elements are depleted. However, other trace elements are largely consistent with the composition of the lower crust as a whole (Fig. 7d).

Figure 7 is about here

6. DISCUSSION

There are two primary divisions among the gabbroic rocks in the south of Qorveh. The first category can sometimes be referred to as "olivine gabbro" even without microscopic examinations since it is lighter in color, contains no amphibole at all, and contains coarse olivines. The second group has amphibole, is darker, and does not contain olivine crystals.

By determining the age of these rocks (Ghalamghash et al., 2018; Azizi et al., 2020), it has been established that these rocks were formed at almost the same time (late Jurassic).

According to the results of Azizi et al.'s (2020) research, the OGRs in the region were formed in an extensional tectonic regime such as a continental rift.

But the AGRs show very different characteristics and features. These rocks are calc-alkaline and have a high content of LIL elements and a low content of HFSEs (Fig. 7a–d). Considering that some elements, like large-ion lithophile elements (LILEs) such as K, Rb, Cs, Sr, Ba, Pb, U, and light rare earth elements (LREEs) are transported by subduction solutions (Stern, 2002; Kelemen et al., 2014;), while others, like high field strength elements (HFSEs), such as Y, Zr, Hf, Nb, Ta, Ti, and heavy rare earth elements (HREEs), are relatively immobile (Stolz et al., 1996; Klemme et al., 2005; Plank et al., 2013;), It can be suggested that the rocks were formed in an active continental margin (subduction) environment.

The oceanic plate dehydrates and discharges fluids in these conditions. These fluids are either produced by the dehydration of hydrous minerals in the subducting plate or by the dehydration of sediments that accompany the subducting sheet (Saunders et al., 1980; Gill, 1981; Tatsumi et al., 1986). The wedge of the metasomatized mantle and some portions of the slab partially melt under these conditions (increasing the amount of fluid phase at constant temperature and pressure) (Stern, 2002). The high partial melting of the source rocks caused by the release of a significant amount of fluid is what causes the samples' high SiO_2 content.
The amount and chemical composition of released fluids depends on the subduction angle, thickness of the subduction slab, and bending curvature (Jarrard, 1986; Lallemand et al., 2005). The authors suggested the existence of a high subduction angle and/or bending curvature.

Depletion of Zr in spider diagrams and low amounts of Zr/Sm and Zr/Ti ratios indicate the formation of magma at a shallow depth (upper parts of the mantle) (Wolde et al., 1996).

Interaction between hydrous basaltic melts and crustal felsic partial melts in the continental arc (CA) occurred via a melting-assimilation-storage-homogenization (MASH) process, as described by Clemens and Stevens (2016).

In the next two sections, we will discuss the magmatic evolution, tectonic setting, and geodynamics of gabbro bodies in the C-SaSZ.

6.1. Magmatic Evolution

Based on the previous works by Azizi et al.'s (2020) differentiation was the only effective process for the magmatic evolution of OGRs.

But to describe the magma evolution of the AGRs, we discuss some factors, including differentiation, fractional crystallization, contamination, magma mixing, and mingling.

The Harker diagrams of major and trace elements show that the source magma has been affected by differentiation (Fig. 6a–l).

Due to the insignificant amount of mg-number of samples, we used the diagrams of La/Sm vs. La (Minster, 1978 and Aldanmaz et al., 2000; Allègre) and Ce/Yb vs. Ce (Davis et al. 2008) to check the presence of fractional crystallization in the process of magma formation. These diagrams determine partial melting as the major factor in

the formation of AGRs (Fig. 8a–b). It seems that at this time, in addition to a compressive regime caused by subduction, an extensional environment behind the arc was also created, which helped magma to rise. The evidence of this extensional environment, including pillow-lava from a back-arc basin at the same age, was reported by Azizi (2018) in the vicinity of the gabbroic bodies. This situation has formed a suitable condition for the partial melting of the mantle.

Figure 8 is about here

The K2O/P2O5 ratio is an index to determine the crustal contamination of basaltic magmas. This is based on the fact that the concentration of potassium is high and that of phosphorus is low in the upper continental crust. As a result, if the continental crust is an important contaminant of basaltic magma, the ratio of these two elements increases.

Mostly, basaltic magmas originating from the mantle have a K2O/P2O5 ratio $\geq$ 2. Crust contamination or apatite fractionation increases this ratio (Hooper, 1982; Carlson & Hart, 1988). The range of changes in the K2O/P2O5 ratio in the AGRs is 4.06-20.2, which suggests magma contamination with the upper crust. In addition, the positive anomaly of Pb, Rb, Ba, Th, and Nd is also common among samples that are relevant to crustal contamination of magma (Rollinson, 1993; Roy et al., 2002; Onwualu-John, 2016; Chen et al., 2021) (Fig. 7a–d).

The coherent behavior of trace elements also suggests that magma mixing and mingling did not play an important role in the formation of rocks. In addition, there is no clear microscopic evidence of magma mixing and mingling (Fig. 6a–l).

6.2. Tectonic Setting and Geodynamics

Based on the geochemical properties of the rocks, such as their high content of LIL elements, low content of HFSEs, insignificant amounts of MgO, FeO, Ni, Cr, Co, and depletion of Zr, it can be concluded that the source magma of the AGRs belongs to a low-depth compressive environment (enriched mantle).

We also employed diagrams of Co vs. Th (Hastie et al., 2007), Ta/Yb vs. Th/Yb and Ta/Yb vs. K2O/Yb (Pearce, 1982), and La/10-Y/15 - Nb/8 (Cabanis et al., 1989) to pinpoint the source of the magma. The samples are all in the calc-alkaline range in the diagrams (Fig. 9a–d). The rocks had an affinity with the active margins field in the Cabanis et al. (1989) diagram, which validates the subduction-related origin of magma. The diagrams also highlight a crucial point: how crustal contamination contributed to the rise in Th concentration in the rocks.

Despite the fact that the back-arc zones share characteristics with the subduction zones, including depletion of heavy trace elements, Ti, Ta, and Nb, and an enrichment of large ion lithophile elements (LILE) and Sr (Pearce et al., 1984), There are differences between these two forms of magma. Contrary to back-arc zones, subduction-related magmas have high Ba/Nb, Ce/Th (Chen et al., 2021), and Ba/la (Escrig et al., 2009; Chen et al., 2021) ratio values, which is consistent with our observations.

Figure 9 is about here

Some researchers like Berberian and King, 1981; Moine-Vaziri, 1985; Verdel et al., 2011; Mohajjel et al., 2014;; believe that the Neo-Tethys Ocean subducted under the Arabian Plate and the Iranian Plateau, which caused the process of partial melting of the mantle, the formation of magma, and consequently the rises and storage of magma, which is the source of AGRs and other igneous rocks in the region (except OGRs).

Figure 10 is about here

In this area, a rift and consequently a back-arc basin were formed almost simultaneously with this process. This rifting has reduced the pressure on the underlying rocks and caused partial melting of the mantle (depleted mantle). The resulting alkaline magma rises and goes through the assimilation-storage-homogenization process (ASH) to form alkaline gabbroic bodies (OGRs) in the region (Fig. 10a–b).

7. CONCLUSIONS

Two kinds of mafic rocks of various origins can be found in southern Ghorveh. Due to the discharge of fluids from the subducting slab, the magma that creates the AGRs originated from an enriched mantle at a shallow depth (upper sections of the mantle). The closure of the Neo-

Tethys Ocean (late Jurassic) was the cause of this process.

A rift and a back-arc basin parallel to the Neo-Tethys Ocean were produced by ascending magma. This fracture has relieved pressure on the deeper portions, which has led to partial melting of the mantle (depleted mantle). The ensuing alkaline magma rose and created gabbroic rocks with high Mg# that have no signs of subduction features (OGRs).

ACKNOWLEDGMENTS

We would like to thank F. Hesami, H. karami, and A. Janani for their fieldwork and technical assistance. We also thank the employees and managers of Kansaran Binalud Company who provided us with their laboratories for chemical analysis.

REFERENCES

Abdulzahra, I.K., Hadi, A., Asahara, Y., Azizi, H., and Yamamoto, K., 2016, Zircon U-Pb ages and geochemistry of Devonian A-type granites in the Iraqi Zagros suture zone (Damamna area): New evidence for magmatic activity related to the Hercynian orogeny. Lithos, 264, 360–374.

https://doi.org/10.1016/j.lithos.2016.09.006

Agard, P., Omrani, J., Jolivet, L., and Mouthereau, F., 2005, Convergence history across Zagros (Iran): constraints from collisional and earlier deformation. International Journal of Earth Sciences, 94, 401–419.

https://doi.org/10.1007/s00531-005-0481-4

Agard, P., Omrani, J., Jolviet, L., Whitechurch, H., Vrielynck, B., Spakman, W., Monie, P., Meyer, B., and Wortel, R., 2011, Zagros orogeny: a subduction-dominated process. Geological Magazine, 148, 692–725.

https://doi:10.1017/S001675681100046X

Ahadnejad, V., Valizadeh, M.V., Deevsalar, R., and Rezaei-Kahkhaei, M., 2011, Age and geotectonic position of the Malayer granitoids: Implication for plutonism in the Sanandaj-Sirjan zone, W Iran. Neues Jahrbuch für Geologie und Paläontologie, 261, 61–75.

https://doi.org/10.1127/0077-7749/2011/0149

Ahmadi-Khalaji, A., Esmaeily, D., Valizadeh, M.V., and Rahimpour-Bonab, H., 2007, Petrology and geochemistry of the granitoid complex of Boroujerd, Sanandaj-Sirjan zone, western Iran. Journal of Asian Earth Sciences, 29, 859–877.

https://doi.org/10.1016/j.jseaes.2006.06.005

Alavi, M., 1980, Tectonostratigraphic evolution of Zagrosides of Iran. Geology, 8, 144–149.

https://doi.org/10.1130/0091-7613(1980)8%3C144:TEOTZO%3E2.0.CO;2

Alavi, M., 1994, Tectonics of Zagros orogenic belt of Iran, new data and interpretation. Tectonophysics, 229, 211–238.

https://doi.org/10.1016/0040-1951(94)90030-2

Aldanmaz, E., Pearce, J., Thirlwall, M., and Mitchell, J., 2000, Petrogenetic evolution of late Cenozoic, post-collision volcanism in western Anatolia, Turkey. Journal of Volcanology and Geothermal Research, 102, 67–95.

https://doi.org/10.1016/S0377-0273(00)00182-7

Alirezaei, S., and Hassanzadeh, J., 2012, Geochemistry and zircon geochronology of the Permian A-type Hasanrobat granite, Sanandaj-Sirjan belt: a new record of the Gondwana break-up in Iran. Lithos, 151, 122–134.

https://doi.org/10.1016/j.lithos.2011.11.015.

Allègre C.J., and Minster J.F., 1978, Quantitative models of trace element behavior in magmatic processes. Earth and Planetary Science Letters, 38, 1–25.

https://doi.org/10.1016/0012-821X(78)90123-1

Allen, M.B., and Armstrong, H.A., 2008, Arabia-Eurasia collision and the forcing of mid-Cenozoic global cooling. Palaegeography, Palaeoclimatology, Palaeoecology, 265, 52–58.

https://doi.org/10.1016/j.palaeo.2008.04.021

Azizi, H., and Asahara, Y., 2013, Juvenile granite in the Sanandaj-Sirjan zone, NW Iran: Late Jurassic-Early Cretaceous arc-continent collision. International Geology Review, 55, 1523–1540.

https://doi.org/10.1080/00206814.2013.782959

Azizi, H., Asahara, Y., Minami, M., and Anma, R., 2020, Sequential magma injection with a wide range of mixing and mingling in Late Jurassic plutons, southern Ghorveh, western Iran. Journal of Asian Earth Sciences, 200, 1–52.

https://doi.org/10.1016/j.jseaes.2020.104469

Azizi, H., Hadad, S., Stern, R.J., and Asahara, Y., 2019a, Age, geochemistry, and emplacement of the ~40-Ma Baneh granite-appinite complex in a transpressional tectonic regime, Zagros suture zone, northwest Iran. International Geology

Review, 61, 195–223.

https://doi.org/10.1080/00206814.2017.1422394

Azizi, H., Kazemi, T., and Asahara, Y., 2017, A-type granitoid in Hasansalaran complex, northwestern Iran: Evidence for extensional tectonic regime in northern Gondwana in the Late Paleozoic. Journal of Geodynamics, 108, 56–72.

https://doi.org/10.1016/j.jog.2017.05.003

Azizi, H., Najari, M., Asahara, Y., Catlos, E.J., Shimizu, M., and Yamamoto, K., 2015, U-Pb zircon ages and geochemistry of Kangareh and Taghiabad mafic bodies in northern Sanandaj-Sirjan zone, Iran: Evidence for intra-oceanic arc and back-arc tectonic regime in Late Jurassic. Tectonophysics, 660, 47–64.

https://doi.org/10.1016/j.tecto.2015.08.008

Azizi, H., and Stern, R.J., 2019, Jurassic igneous rocks of the central Sanandaj-Sirjan zone (Iran) mark a propagating continental rift, not a magmatic arc. Terra Nova, 31, 415–423. https://doi.org/10.1111/ter.12404

Azizi, H., Stern, R.J., Topuz, G., Asahara, Y., and Shafaii Moghadam, H., 2019b. Late Paleocene adakitic granitoid from NW Iran and comparison with adakites in the NE Turkey: Adakitic melt generation in normal continental crust. Lithos, 346–347, 31–48.

https://doi.org/10.1016/J.Lithos.2019.105151

Azizi, H., Zanjefili-Beiranvand, M., and Asahara, Y., 2015, Zircon U-Pb ages and petrogenesis of a tonalite-trondhjemite-granodiorite (TTG) complex in the northern Sanandaj-Sirjan zone, northwest Iran: Evidence for Late Jurassic arc-continent collision. Lithos, 216, 178–195.

https://doi.org/10.1016/j.lithos.2014.11.012

Babaie, H.A., Ghazi, A.M., Babaie, A., La-Tour, T.E., and Hassanipak, A.A., 2000, Geochemistry of arc volcanic rocks of the Zagros crush zone, Neyriz, Iran. Journal of Asian Earth Sciences, 19, 61–76.

https://doi.org/10.1016/S1367-9120(00)00012-2

Ballato, P., Uba, C.E., Landgraf, A.,Strecker, M.R., Sudo, M., Stockli, D., Friedrich, A., and Tabatabaei, S.H., 2011, Arabia-Eurasia continental collision: insights from late Tertiary foreland basin evolution in the Alborz Mountains, northern Iran. Geological Society of America Bulletin, 123, 106–131.

https://doi.org/10.1130/B30091.1

Bayati, M., Esmaeily, D., Maghdour-Mashhour, R., Li, X.H., and Stern, R.J., 2017, Geochemistry and petrogenesis of Kolah-Ghazi granitoids of Iran: Insights into the Jurassic Sanandaj-Sirjan magmatic arc. Geochemistry, 77, 281–302. https://doi.org/10.1016/j.chemer.2017.02.003.

Bea, F., Mazhari, A., Montero, P., Amini, S., and Ghalamghash, J., 2011, Zircon dating, Sr and Nd isotopes, and element geochemistry of the Khalifan pluton, NW Iran: Evidence for Variscan magmatism in a supposedly Cimmerian superterrane. Journal of Asian Earth Sciences, 40, 172–179.

https://doi.org/10.1016/j.jseaes.2010.08.005

Berberian, M., 1995, Master blind thrust faults hidden under the Zagros folds: active basement tectonics and surface morphotectonics. Tectonophysics, 241, 193–224.

https://doi.org/10.1016/0040-1951(94)00185-C

Berberian, M., and King, G.C.P., 1981, Toward a paleogeography and tectonic evolution of Iran. Canadian Journal of Earth Sciences, 18, 210–265.

https://doi.org/10.1139/e81-019

Bird, P., 1978, Finite element modeling of lithosphere deformation: the Zagros collision orogeny. Tectonophysics, 50, 307–336.

https://doi.org/10.1016/0040-1951(78)90140-3

Bushara, M.N., 1995, Subsurface structure of the eastern edge of the Zagros Basin as inferred from gravity and satellite data. AAPG Bulletin, 79, 1259–1274.

https://doi.org/10.1306/7834D49A-1721-11D7-8645000102C1865D

Cabanis, B., and Lecolle, M., 1989, Le diagramme La/10-Y/15-Nb/8: The La/10-Y/15-Nb/8 diagram: a tool for discrimination volcanic series and evidencing continental crust magmatic mixtures and/or contamination. Comptes rendus de l'Académie des sciences.Série 2, Mécanique, Physique, Chimie, Sciences de l'univers, Sciences de la Terre, 309, 2023–2029. (In French)

Carlson, R.W., and Hart, W.K., 1988, Continental Flood Basalts (3rd edition). Springer- Dordrecht, California, 60 p.

https://doi.org/10.1007/978-94-015-7805-9_2

Cawthorn, R.G., and Walraven, F., 1998, Emplacement and Crystallization Time for the Bushveld Complex. Journal of Petrology, 39, 1669–1687.

https://doi.org/10.1093/petroj/39.9.1669

Chen, S.S., Hou, T., Liu, J.Q., Zhang, Z.C., 2021, Geochemical Variation of Miocene Basalts within Shikoku Basin: Magma Source Compositions and Geodynamic Implications. Minerals, 11, 35–68.

https://doi.org/10.3390/min11010025

Chiu, H.Y., Chung, S.L., Zarrinkoub, M.H., Mohammadi, S., Khatib, M.M., and Iizuka, Y., 2013, Zircon U-Pb age constraints from Iran on the magmatic evolution related to Neotethyan subduction and Zagros orogeny. Lithos, 162–163, 70–87.

https://doi.org/10.1016/j.lithos.2013.01.006

Claeson, D., and Meurer, W., 2004, Fractional crystallization of hydrous basaltic ‘‘arc-type’’ magmas and the formation of amphibole-bearing gabbroic cumulates. Contributions to Mineralogy and Petrology, 147, 288–304

https://doi.org/10.1007/s00410-003-0536-0

Clemens, J.D., and Stevens, G., 2016, Melt segregation and magma interactions during crustal melting: Breaking out of the matrix. Earth-Science Reviews, 160, 333–349. https://doi.org/10.1179/1743275813y.0000000023.

Daneshvar, N., Maanijou, M., Azizi, H., and Asahara, Y., 2019, Petrogenesis and geodynamic implications of an Ediacaran (550 Ma) granite complex (metagranites), southwestern Saqqez, northwest Iran. Journal of Geodynamics, 132, 1–58.

https://doi.org/10.1016/j.jog.2019.101669

Davis, A., Cousens, B.L., Keaten, R., and Paduan, J.B., 2008, Geochemistry of basalt from the North Gorda segment of the Gorda Ridge: Evolution toward ultraslow spreading ridge lavas due to decreasing magma supply. Geochemistry, Geophysics, Geosystems, 9, 30–54.

https://doi.org/10.1029/2007GC001775

Deevsalar, R., Shinjo, R., Ghaderi, M., Murata, M., Hoskin, P.W.O., Oshiro, S., Wang, K.L., Lee, H.Y., and Neill, I., 2017, Mesozoic-Cenozoic mafic magmatism in Sanandaj-Sirjan zone, Zagros orogen (Western Iran): Geochemical and isotopic inferences from Middle Jurassic and Late Eocene gabbros. Lithos, 284–285, 588–607. https://doi.org/10.1016/J.lithos.2017.05.009

Deevsalar, R., Shinjo, R., Liégeois, J.P., Valizadeh, M.V., Ahmadian, J., Yeganehfar, H., Murata, M., and Neill, I., 2018, Subduction-related mafic to felsic magmatism in the Malayer-Boroujerd plutonic complex, western Iran. Swiss Journal of Geosciences, 111, 269–293.

https://doi.org/10.1007/s00015-017-0287-y

Escrig, S. Bézos, A., Goldstein, S.L., Langmuir, C.H., and Michael, P.J. 2009, Mantle source variations beneath the Eastern Lau Spreading Center and the nature of subduction components in the Lau basin-Tonga arc system. Geochemistry, Geophysics, Geosystems, 10, 11–43.

https://doi.org/10.1029/2008GC002281.

Esna-Ashari, A., Tiepolo, M., Valizadeh, M.V., Hassanzadeh, J., and Sepahi, A.A., 2012, Geochemistry and zircon U-Pb geochronology of Aligoodarz granitoid complex, Sanandaj-Sirjan zone, Iran. Journal of Asian Earth Sciences, 43, 11–22.

https://doi.org/10.1016/j.jseaes.2011.09.001

Sabzai, M., Eshraghi, S.A., and Roshan-Ravan, J., 1997, Geological map of Sirjan (1: 100,000). Geological Survey of Iran, 21, 43-56 (in Farsi with an English abstract).

Ghalamghash, J., Houshmand, S., Sheikh Zakaraiee, S.J., and Rashid, H., 2018, Ar/Ar dating, geochemistry and petrogenesis of Khersrah intrusive mass. Scientific Quarterly Journal of Geosciences, 29, 135-144. (in Farsi with an English abstract).

https://doi.org/10.22071/gsj.2018.116501.1393

Ghalamghash, J., Mirnejad, H., and Rashid, H., 2009, Magma mixing and mingling patterns along Neo-Tethys continental margin, Sanandaj-Sirjan zone, NW Iran: a case study from Alvand pluton. Neues Jahrbuch Fur Mineralogie, 186, 79–93.

https://doi.org/10.1127/0077-7757/2009/0133

Gill, J.B., 1981, Orogenic Andesite and Plate Tectonics. Springer-Verlag, Berlin, 390 p. https://doi.org/10.1007/978-3-642-68012-0

Shafaii-Moghadam, H., Li, X., Ling, X., Stern, R., Santos, J.F., Meinhold, G., Ghorbani, Gh., and Shahabi, Sh., 2015, Petrogenesis and tectonic implications of Late Carboniferous A-type granites and gabbronorites in NW Iran: Geochronological and geochemical constraints. Lithos, 212–215, 266–279.

https://doi.org/10.1016/j.lithos.2014.11.009

Hastie, A.R., Kerr, A.C., Pearce, J.A., and Mitchell, S.F., 2007, Classification of altered volcanic island arc rocks using immobile trace elements: development of the Th Co discrimination diagram. Journal of Petrology, 48,

2341–2357.

https://doi.org/10.1093/petrology/egm062

Hooper, P.R., 1982, The Columbia River Basalts. Science, 215, 1463-1468. https://doi.org/10.1126/science.215.4539.1463

Jarrard, R.D., 1986, Relations among subduction parameters. reviews of geophysics, 24, 217–284.

https://doi.org/10.1029/RG024i002p00217

Kelemen, P.B., Hanghoj, K., and Greene, A.R., 2007, One view of the geochemistry of subduction-related magmatic arcs, with an emphasis on primitive andesite and lower crust. Treatise on Geochemistry, 3, 749–805.

https://doi.org/10.1016/B0-08-043751-6/03035-8

Klemme, S., Prowatke, S., Hametner, K., and Günther, D., 2005, Partitioning of trace elements between rutile and silicate melts: implications for subduction zones. Geochimica et Cosmochimica Acta, 69, 2361–2371.

https://doi.org/10.1016/j.gca.2004.11.015.

Lallemand, S., Heuret, A., and Boutelier, D., 2005, On the relationship between slab dip, back-arc stress, upper plate absolute motion, and crustal nature in subduction zones. Geochemistry, Geophysics, Geosystems, 6, 18–36.

https://doi.org/10.1029/2005GC000917

Lechmann, A., Burg, J.P., Ulmer, P., Mohammadi, A., Guillong, M., and Faridi, M., 2018, From Jurassic rifting to Cretaceous subduction in NW Iranian Azerbaijan: geochronological and geochemical signals from granitoids. Contributions to Mineralogy and Petrology, 173, 54–70.

https://doi.org/10.1007/s00410-018-1532-8

Mahmoudi, S., Corfu, F., Masoudi, F., Mehrabi, B., and Mohajjel, M., 2011, U-Pb dating and emplacement history of granitoid plutons in the northern Sanandaj-Sirjan zone, Iran. Journal of Asian Earth Sciences, 41, 238–249.

https://doi.org/10.1016/j.jseaes.2011.03.006

Mazhari, S.A., Amini, S., Ghalamghash, J., and Bea, F., 2011, Petrogenesis of granitic unit of naqadeh complex, Sanandaj-Sirjan zone, NW Iran. Arabian Journal of Geosciences, 4, 59–67.

https://doi.org/10.1007/s12517-009-0077-6

Mazhari, S.A., Bea, F., Amini, S., Ghalamghash, J., Molina, J.F., Montero, P., Scarrow, J.H., and Williams, I.S., 2009, The Eocene bimodal Piranshahr massif of the Sanandaj-Sirjan zone, NW Iran: a marker of the end of the collision in the Zagros orogeny. Journal of the Geological Society of London, 166, 53–69.

https://doi.org/10.1144/0016-76492008-022

McCallum, I.S., 1996, The Stillwater Complex. Developments in Petrology, 15, 441–483.

https://doi.org/10.1016/S0167-2894(96)80015-7

Middlemost, E.A.K., 1994, Naming materials in the magma/igneous rock system. Earth-Science Reviews, 37, 215–224.

https://doi.org/10.1016/0012-8252(94)90029-9

Moghadam, H.S., Li, X.H., Ling, X.X., Stern, R.J., Santos, J.F., Meinhold, G., Ghorbani, G., and Shahabi, S., 2015, Petrogenesis and tectonic implications of Late Carboniferous A-type granites and gabbronorites in NW Iran: Geochronological and geochemical constraints. Lithos, 212–215, 266–279.

https://doi.org/10.1016/j.lithos.2014.11.009

Mohajjel, M., and Fergusson, C.L., 2000, Dextral transpression in Late Cretaceous continental collision, Sanandaj-Sirjan zone, western Iran. Journal of Structural Geology, 22, 1125–1139.

https://doi.org/10.1016/S0191-8141(00)00023-7

Mohammadi, A., Moazzen, M., Lechmann, A., and Laurent, O., 2019, Zircon U-Pb geochronology and geochemistry of Late Devonian–Carboniferous granitoids in NW Iran: implications for the opening of Paleo-Tethys. International Geology Review, 62, 1–18. https://doi.org/10.1080/00206814.2019.1675540

Mohammadi, N., Sodoudi, F., Mohammadi, E., and Sadidkhouy, A., 2013, New constraints on lithospheric thickness of the Iranian plateau using converted waves. Journal of Seismology, 17, 883–895.

https://doi.org/10.1007/s10950-013-9359-2

Mollaei Yeganeh, T., Torkian, A., and Sepahi, A.A., 2017, Source and geothermobarometry of the gabbrodioritic intrusive body, (S-Qorveh-Kurdistan); with emphasis on minerals chemistry. Iranian Journal of Crystallography and Mineralogy, 25, 153–166. (in farsi with English abstract)

Moradi, A., Shabanian, N., Davoudian, A.R., Azizi, H., Santos, J., and Asahara, Y., 2020, Geochronology and petrogenesis of the Late Neoproterozoic granitic gneisses of Golpayegan Metamorphic Complex: A new respect for Cadomian crust in the Sanandaj-Sirjan zone, Iran. International Geology Review, 64, 1450–1473.

https://doi.org/10.1080/00206814.2020.1821251

Mungall, J.E., Kamo, S.L., and McQuade, S., 2016, U-Pb geochronology documents out-of-sequence emplacement of ultramafic layers in the Bushveld Igneous Complex of South Africa. Nature Communications, 7, 50–63.

https://doi.org/10.1038/ncomms13385

Nabavi, M.H., 1976, An introduction to the geology of Iran. Geological Survey of Iran, 3, 109–117. (in Farsi).

Onwualu-John J.N., 2016, Positive anomalous concentrations of Pb in some gabbroic rocks of Afikpo basin southeastern Nigeria. Environmental geochemistry and health, 38, 1029–1035.

https://doi.org/10.1007/s10653-016-9817-1

Pearce, J.A., 1982, Trace element characteristics of lavas from destructive plate boundaries. John Wiley and Sons, 5, 525–548.

Pearce, J.A., 1983, Role of the sub-continental lithosphere in magma genesis at active continental margins. Continental Basalts and Mantle Xenoliths, 17, 230–249.

Plank, T., Kelley, K.A., Zimmer, M.M., Hauri, E.H., and Wallace, P.J., 2013, Why do mafic arc magmas contain 4wt% water on average? Earth and Planetary Science Letters, 364, 168–179.

https://doi.org/10.1016/j.epsl.2012.11.044.

Rollinson, H.R., 1993, Using geochemical data: Evaluation, presentation, interpretation. Wiley, 193 p.

Roy, A., Sarkar, A., Jeyakumar, S., Aggrawap, S., and Ebihara, M., 2002, Mid-proterozoic plume-related thermal event in eastern Indian craton: evidence from trace elements, REE geochemistry and Sr-Nd isotope systematics of basic-ultrabasic intrusives from Dalma volcanic belt. Gondwana Research, 5, 133–145.

https://doi.org/10.1016/S1342-937X(05)70897-2

Sabeti, M., Emami M.H. Saeedi, A., Ajdary, K. Minaee, A., and Nadimi, A.R. 2012, Petrological, geochemical and tectonomagmatic setting of Boein- Miandasht intrusion in Sanandaj- Sirjan zone (SSZ) (west of Iran). Scientific Quarterly Journal, 21, 43–56. (in farsi with English abstract)

https://doi.org/10.22071/gsj.2012.53955

Saki, A., 2010, Proto-Tethyan remnants in northwest Iran: geochemistry of the gneisses and metapelitic rocks. Gondwana Research, 17, 704–714.

https://doi.org/10.1016/j.gr.2009.08.008

Salters, V., and Stracke, A., 2004, Composition of the depleted mantle. Geochemistry, Geophysics, Geosystems, 5, 1–27.

https://doi.org/10.1029/2003GC000597

Saunders, A.D., Tarney, J., and Weaver, S.D., 1980, Transverse geochemical variations across the Antarctic peninsula: implications for the genesis of calc-alkaline magmas. Earth and Planetary Science Letters, 46, 344–60.

https://doi.org/10.1016/0012-821X(80)90050-3

Sengor, A.M.C., 1990, A new model for the Late Paleozoic-Mesozoic tectonic evolution of Iran and implications for Oman. Geological Society, London, Special Publication 49, 797–831.

https://doi.org/10.1144/GSL.SP.1992.049.01.49

Sepahi, A., Shahbazi, H., Siebel, W., and Ranin, A., 2014, Geochronology of plutonic rocks from the Sanandaj-Sirjan zone, Iran and new zircon and titanite U-Th-Pb ages for granitoids from the Marivan pluton. Geochronometria, 41, 207–215. https://doi.org/10.2478/s13386-013-0156-z

Shabanian, N., Davoudian, A.R., Azizi, H., Asahara, Y., Neubauer, F., Genser, J., Dong, Y., and Lee, J.K., 2020, Petrogenesis of the Carboniferous Ghaleh-Dezh metagranite, Sanandaj-Sirjan zone, Iran: constraints from new zircon U-Pb and 40Ar/39 Ar ages and Sr-Nd isotopes. Geological Magazine, 157, 1–30.

https://doi.org/10.1017/S0016756820000096

Shabanian, N., Davoudian, A.R., Dong, Y., and Liu, X., 2018, U-Pb zircon dating, geochemistry and Sr-Nd-Pb isotopic ratios from Azna-Dorud Cadomian metagranites, Sanandaj-Sirjan zone of western Iran. Precambrian Research, 306, 41–60. https://doi.org/10.1016/j.precamres.2017.12.037

Shafaii Moghadam, H., Griffin, W.L., Li, X.H., Santos, J.F., Karsli, O., Stern, R.J., Ghorbani, G., Gain, S., Murphy, R., and O'Reilly, S.Y., 2017, Crustal evolution of NW Iran: Cadomian Arcs, Archean fragments and the Cenozoic magmatic flare-up. Journal of Petrology, 58, 2143–2190.

https://doi.org/10.1093/petrology/egy005

Shakerardakani, F., Li, X.H., Neubauer, F., Ling, X.X., Li, J., Monfaredi, B., and Wu, L.G., 2020, Genesis of early cretaceous leucogranites in the Central Sanandaj-Sirjan zone, Iran: reworking of Neoproterozoic metasedimentary rocks in an active continental margin. Lithos, 352, 1–61.

https://doi.org/10.1016/j.lithos.2019.105330

Stern, R.J., 2002, Subduction zones. Reviews of Geophysics, 40, 3–38.

https://doi.org/10.1029/2001RG000108

Stöcklin, J., and Nabavi, M.H., 1973, Tectonic Map of Iran, Scale 1:2500000, Geological Survey of Iran, Tehran.

Stolz, A.J., Jochum, K.P., Spettel, B., and Hofmann, A.W., 1996, Fluid- and melt-related enrichment in the sub-arc mantle: Evidence from Nb/Ta variations in island-arc basalts. Geology, 24, 587–590.

https://doi.org/10.1130/0091-7613(1996)024%3C0587:FAMREI%3E2.3.CO;2

Tatsumi, Y., Hamilton, D.L., and Nesbitt, R.W., 1986, Chemical characteristics of fluid phase released from a subducted lithosphere and origin of arc magmas: evidence from high-pressure experiments and natural rocks. Journal of Volcanology and Geothermal Research, 29, 293–309.

https://doi.org/10.1016/0377-0273(86)90049-1

Verdel, C., Wernicke, B.P., Hassanzadeh, J., and Guest, B., 2011, A Paleogene extensional flareup in Iran. Tectonics, 30, 52–72.

https://doi.org/10.1029/2010TC002809

Willbold, M., and Stracke, A., 2010, Formation of enriched mantle components by recycling of upper and lower continental crust. Chemical Geology, 276, 188–197.

https://doi.org/10.1016/j.chemgeo.2010.06.005

Wolde, B., Asres, Z., Desta, Z., and Gonzalez, J., 1996, Neoproterozoic zirconium-depleted boninite and tholeiitic series rocks from Adola, southern Ethiopia. Precambrian Research, 80, 261–279.

https://doi.org/10.1016/S0301-9268(96)00018-6

LIST OF TABLES AND FIGURES

Table 1. Whole rocks chemical compositions of ABGs intrusive bodies in the southern Ghorveh

Fig. 1. Geological map of Iran (Alavi, 1994; Stöcklin and Nabavi, 1973) showing the location of sanandaj - sirjan structural zone.

Fig. 2. Geological map of southern Ghorveh (Eshraghi et al., 1996) and sample locations. ABGs (right) and OBGs (left) in the bottom and show an almost linear structure. The main host rock is the Ghorveh-Songhor metamorphic complex of a Jurassic age. Some contact metamorphism overprints on the Jurassic metamorphic complex are due to the injection of intrusive bodies during the Late Jurassic.

Fig. 3. (a–d) Field outcrops of ABGs in southern Ghorveh. The ABGs formed some low hills with a mound shape morphology.

Fig. 4. Micrographic photos of ABGs in southern Ghorveh. (a–p) ABGs with granular textures as well as main minerals (e.g., plagioclase, clinopyroxene) and minor minerals (hornblende and biotite). (a–d) Different sizes plagioclases in some cases with albite-pericline and Carlsbad twins. (4e–p) Automorphic to amorphous pyroxenes (in certain cases with twining and ophitic textures), and the alteration products include amphibole, biotite, opaque minerals, and chlorite. (g–p) Plagioclases whit albite-pericline twins, Carlsbad twins, and normal zoning; and the alteration products include sericite and calcite. In plagioclases with zoning, alteration to sericite can be seen in the central parts.

Fig. 5. Whole-rock compositions of the intrusive bodies in southern Ghorveh. In the diagram of Cox et al (1979), the samples are plotted in the gabbroic field.

Fig. 6. Harker diagrams for major and trace elements. See the text for more details.

Fig. 7. Chemical compositions normalized by chondrite (Thompson, 1982), primitive mantle (McDonough and Sun, 1995), MORB (Pearce, 1983), and lower crust (Weaver and Tarney, 1984).

Fig. 8. (a) La/Sm vs. La diagram for the ABGs. (b) Ce/Yb versus Ce abundance shows trends compatible with varying degrees of partial melting.

Fig. 9. Discrimination diagrams for the tectonic setting of the Jurassic intrusive bodies in southern Ghorveh. Co vs. Th (Hastie et al., 2007), Ta/Yb vs. Th/Yb and Ta/Yb vs. K2O/Yb (Pearce, 1982), and La/10- Y/15 - Nb/8 (Cabanis et al., 1989), show that the ABGs group has some affinity for active margins type magmatism.

Fig. 10. A schematic model for the development of magma in intrusive bodies in southern Ghorveh. The

model shows subcontinental lithospheric mantle (SCLM) as the source of mafic bodies. (a) During the first stage, calc-alkaline magma was injected into the upper continent, near the surface which causes the formation of a rift. (b) During the second stage, alkaline magma rises and goes through the assimilation-storage-homogenization process (ASH) and was injected into the upper continent, near the surface to form alkaline gabbroic bodies (OGRs) in the region (The image modified and used from Wikimedia Commons by K. D. Schroeder, CC-BY-SA 4.0. The original file is available as Subduction-en.svg). **Table 1.** Whole rocks chemical compositions of ABGs intrusive bodies in the southern Ghorveh.

Sample	Unite	Gbs 1	Gbs 2	Gbs 6	Gbs 14	Gbs 16	Gbs 23	Gbs 29	Gbs 35	Gbs 39	Gbs 44	Gbs 50	Gbs 53	KH G1	KH G2	KH G3
Major oxide									**ABGs**							
SiO2	%	52,25	52,37	52,01	—	—	—	—	—	52,1	—	—	—	52,21	52,57	52,54
TiO2	%	0,976	0,993	1,038	—	—	—	—	—	0,994	—	—	—	0,986	0,941	0,918
Al2O3	%	15,37	15,43	14,84	—	—	—	—	—	15,42	—	—	—	15,94	15,96	16,37
Fe2O3	%	8,89	8,79	9,07	—	—	—	—	—	8,95	—	—	—	8,8	8,55	8,75
MnO	%	0,119	0,136	0,127	—	—	—	—	—	0,11	—	—	—	0,12	0,127	0,107
MgO	%	6,76	6,79	6,57	—	—	—	—	—	6,59	—	—	—	6,14	6,62	6,04
CaO	%	9,37	9,36	10,2	—	—	—	—	—	9,48	—	—	—	9,51	9,27	9,07
Na2O	%	1,03	1,11	0,93	—	—	—	—	—	1,06	—	—	—	0,97	1,39	1,31
K2O	%	1,48	1,36	1,56	—	—	—	—	—	1,54	—	—	—	1,51	1,19	1,26
P2O5	%	0,179	0,138	0,159	—	—	—	—	—	0,17	—	—	—	0,16	0,188	0,141
LOI	%	1,89	1,88	2,15	—	—	—	—	—	2,63	—	—	—	2,19	1,33	2,03
Total	%	98,314	98,357	98,654	—	—	—	—	—	99,044	—	—	—	98,536	98,136	98,536
Trace elements																
Sc	ppm	24,4	25,5	24,5	25,8	23,9	24,1	24	25,7	24,9	22,2	24,3	24	25,5	42,2	29,7
V	ppm	356	384	345	368	348	339	389	346	356	333	375	359	374	351	360
Cr	ppm	153	162	170	174	158	119	154	260	193	219	189	177	183	69	231
Co	ppm	19,21	17,43	17,66	18,43	15,2	17,98	15,42	17,71	16,47	15,36	17,8	16,69	15,56	20,4	18,37
Ni	ppm	211	203	241	233	208	239	221	257	217	222	214	254	275	245	263
Cu	ppm	9,3	20,6	31,6	19,8	22,4	19,2	36,4	35,1	22,4	31,7	78,4	21,3	12,3	18	16,6
Zn	ppm	41,7	44,8	40,9	42,1	38,3	37,1	38,1	34,2	42,1	55,6	42	44,9	66,9	93,5	257,6
Rb	ppm	56,66	65,3	75,61	54,47	62,1	58,25	91,21	58,2	84,29	89,28	65,22	67,54	90,19	82,4	73,1
Sr	ppm	253,7	265,3	278,3	255,4	309,9	311,1	319,8	303,1	311	301,5	269,3	322,7	246,8	272,3	322,6
Zr	ppm	13	15	15	16	12	13	13	12	15	18	16	13	19	25	22
Nb	ppm	2,81	3,2	2,83	3,17	3,13	2,8	3,2	2,65	2,8	2,54	2,69	2,41	2,56	2,56	2,37
Cs	ppm	3,68	3,64	2,6	3,6	3,2	3,2	3,3	3	3,1	3,67	3,5	2,4	4,1	3,6	3,73
Ba	ppm	116,7	140,9	122	130	112,8	130,3	125,3	105,6	119,7	157,2	136,9	104,1	132,8	78,4	64,8
Pb	pp	4,64	4,29	3,66	4,11	3,86	3,01	4,52	6,28	4,2	6,17	5,15	6,64	2,26	5,79	4,12

	m															
Th	**ppm**	3,9	4,3	4	3,8	3,2	3,8	3,8	3	4	3,2	4,4	4,1	3,4	3,57	3,66
U	**ppm**	1,03	1,14	1,14	1,03	1,03	1,03	1,03	1,03	1,03	1,14	1,03	0,96	0,96	0,64	0,7
Hf	**ppm**	6,34	6,35	5,22	7,43	6,52	4,64	6,74	2,89	4,47	5	4,8	5	5,3	5,3	5,8
Ta	**ppm**	0,93	0,93	0,82	0,89	0,87	0,71	0,93	0,55	0,65	0,61	0,85	0,81	0,93	0,97	0,87
Y	**ppm**	14,5	14,9	15,3	17,5	15,3	16,3	16,9	16,3	16,9	15,4	16,2	15,7	15,9	15,6	15,4
Rare earth elements																
La	**ppm**	12,8	11,3	10,83	11,87	10,87	12,41	11,74	11,7	11,7	12,37	13,05	12,41	12,63	11,7	11,43
Ce	**ppm**	29,83	22,51	22,9	25,67	19,52	25,91	28,54	18,3	31,3	28,22	27,17	25	26,1	12,88	19,15
Pr	**ppm**	7,87	6,92	6,97	7,24	6,22	7,35	7,3	6,21	7,89	7,21	7,3	7	7,28	5,51	5,6
Nd	**ppm**	13,59	13,16	12,8	13,93	13,17	14	14,15	13,7	14,6	13,25	14	13,37	13,6	13,7	14
Sm	**ppm**	6,17	5,71	5,63	5,78	4,6	5,6	5,74	4,55	6	5,39	5,8	5,22	5,61	4,3	4,17
Eu	**ppm**	2,61	2,69	2,54	2,57	2,2	2,63	2,47	2,2	2,59	2,53	2,5	2,44	2,55	2,12	2,19
Gd	**ppm**	4,17	3,98	3,83	2,91	3	3,86	3,99	2,92	4,11	3,65	3	3,54	2,86	3	2,7
Tb	**ppm**	1,41	1,17	1,31	1,79	2,14	1,93	1,67	1,42	1,64	1,91	1,75	1,54	1,48	1,22	1,83
Dy	**ppm**	2,63	2,75	2,81	2,89	2	2,76	2,82	2,43	2,21	2,66	2,92	2,97	2,74	2,76	2,13
Ho	**ppm**	0,82	0,83	0,82	0,83	0,81	0,82	0,82	0,81	0,83	0,83	0,8	0,82	0,81	0,82	0,79
Er	**ppm**	4,56	4,8	4,19	4,92	4,59	3,98	4,67	3,28	3,92	3	3	3,4	3,3	3,3	3,6
Tm	**ppm**	0,71	0,61	0,52	0,89	0,76	0,64	0,72	0,56	0,67	0,73	0,71	0,74	0,69	0,51	0,68
Yb	**ppm**	1,27	1,29	1,28	1,3	1,3	1,29	1,28	1,33	1,29	1,32	1,35	1,31	1,34	1,31	1,3
Lu	**ppm**	0,7	0,73	0,63	0,79	0,73	0,6	0,75	0,46	0,57	0,5	0,5	0,6	0,6	0,6	0,6
Mg#		43,19	43,58	42	_	_	_	_	_	42,4	_	_	_	41,09	43,63	40,83

Table 1. Continue.

Sample	**Unite**	**KHG4**	**KHG5**	**KHG6**	**KHG7**	**KHG8**	**KHG9**	**KHG10**	**KHG11**	**KHG12**	**KHG13**	**KHG14**	**KHG15**	**KHG16**	**KHG17**
Major oxide									**ABGs**						
SiO2	%	51,97	52,35	—	—	—	—	—	—	—	52,36	—	—	—	—
TiO2	**%**	1,058	0,943	—	—	—	—	—	—	—	0,925	—	—	—	—
Al2O3	**%**	14,88	15,38	—	—	—	—	—	—	—	15,61	—	—	—	—
Fe2O3	**%**	9,29	8,6	—	—	—	—	—	—	—	8,79	—	—	—	—
MnO	**%**	0,106	0,121	—	—	—	—	—	—	—	0,145	—	—	—	—
Mg	**%**	6,8	6,88	—	—	—	—	—	—	—	6,72	—	—	—	—

O															
CaO	**%**	10,6	9,22	—	—	—	—	—	—	—	9,17	—	—	—	—
Na2O	**%**	0,88	1,1	—	—	—	—	—	—	—	0,95	—	—	—	—
K2O	**%**	1,59	1,47	—	—	—	—	—	—	—	1,37	—	—	—	—
P2O5	**%**	0,121	0,167	—	—	—	—	—	—	—	0,147	—	—	—	—
LOI	**%**	2,28	2,04	—	—	—	—	—	—	—	2,57	—	—	—	—
Total	**%**	99,575	98,271	—	—	—	—	—	—	—	98,757				
Trace elements															
Sc	**ppm**	24,73	21,53	20,27	22,66	21,3	20,93	21,59	22,26	21,22	20,92	24,63	20,61	23,73	21,57
V	**ppm**	376	349	439	411	439	476	499	412	524	527	425	399	385	325
Cr	**ppm**	203	176	180	138	182	178	122	173	175	154	133	218	205	251
Co	**ppm**	20,79	19,47	18,27	17,12	19,97	19,49	20,1	19,33	17,8	19,72	18,6	20,4	20,71	26,13
Ni	**ppm**	243	256	291	251	289	278	264	243	239	287	254	264	271	265
Cu	**ppm**	22,2	21,9	12,8	20,5	22	16,6	16,9	22,5	15,8	11,6	12,1	50,2	12	17,5
Zn	**ppm**	482,8	36,2	53,7	38,8	53,8	46,6	66,4	51,8	52,8	46,4	36,3	42,6	39,5	38,4
Rb	**ppm**	65,3	72,31	71,14	69,27	59,13	82,15	68,1	95,29	791	69,3	75,2	75,23	55,6	59,41
Sr	**ppm**	337	314,8	256,9	325,7	266,7	316,6	255,5	281,4	291,1	280,8	291,4	338,4	303	354,5
Zr	**ppm**	18	18	18	12	19	17	28	17	17	17	13	23	12	13
Nb	**ppm**	2,28	2,22	2,7	2,9	2,51	2,39	2,24	2,1	2,3	2,36	2,43	2,57	2,51	2,3
Cs	**ppm**	3,31	3,84	4,5	3,6	3,3	4,4	3,1	3,45	3,61	2,94	2,96	3,39	3,1	3,52
Ba	**ppm**	68	83,1	140,8	130	137,9	155,6	72,6	129,7	136,2	158,8	117,2	84,7	96,3	80,6
Pb	**ppm**	6,02	4,24	4,11	6,34	4	4,2	4,17	3,85	6,96	5,42	3,99	4,27	6,73	4,61
Th	**ppm**	3,21	4,2	3,2	3,3	3,3	4,5	3,4	3,4	3,5	4,8	3,6	3,9	3,4	3,8
U	**ppm**	0,7	0,59	1	1,03	1,03	1,15	0,77	1,03	1,03	1,03	1,03	1,03	0,62	0,54
Hf	**ppm**	5,5	5,4	5,1	5	5	5	5	5	6	4	4	5	5	5
Ta	**ppm**	0,96	0,84	0,87	0,95	0,91	0,85	0,94	0,93	0,9	0,9	0,8	0,9	0,9	0,99
Y	**ppm**	15,3	15,7	16,3	15	16	17,4	15,1	14,9	15	17	16,5	15,2	15,3	15,1
Rare earth elements															
La	**ppm**	11,3	11,2	13,14	12,12	11,49	11,31	12,2	13,28	13,22	14,49	12,78	11,57	11,5	12,3
Ce	**ppm**	16	19,74	26,46	25,5	24	24,93	19,9	26,48	26,7	32,47	25,92	13,59	20,12	20,17
Pr	**ppm**	5,93	5,6	7,27	6,94	6,96	7,1	5,93	7,1	7,11	8	7,1	5,52	6,3	5,94
Nd	**ppm**	13,6	13,18	13,9	12,5	12,53	13,8	13	13,47	13,3	14,89	14	13,5	13,71	13,14
Sm	**ppm**	4,1	3,76	5,52	5,31	5,5	5,67	4,4	5,54	5,49	6,1	5,63	4	4,67	3,49

Eu	**ppm**	2,23	2,17	2,51	2,67	2,5	2,5	2,28	2,55	2,51	2,6	2,56	2,1	2,24	2,29
Gd	**ppm**	2,8	2,43	3,81	3,56	3,87	3,83	3,13	3,74	3,76	4,21	3,89	2,61	3,12	2,2
Tb	**ppm**	1,4	1,76	1,49	1,61	1,23	1,94	1,38	2,11	1,56	1,62	1,79	1,65	1,82	1,2
Dy	**ppm**	2,64	2,47	2,77	2,51	2,74	2,71	2,1	2,63	2,69	3	2,71	2,54	2,33	2,4
Ho	**ppm**	0,82	0,8	0,79	0,81	0,81	0,79	0,81	0,8	0,83	0,79	0,81	0,79	0,76	0,79
Er	**ppm**	3	3	3,1	3,2	3,3	3,2	3	2,9	3,1	3	2,9	2,9	3	3
Tm	**ppm**	0,63	0,6	0,54	0,61	0,79	0,74	0,52	0,64	0,79	0,66	0,61	0,64	0,69	0,5
Yb	**ppm**	1,27	1,39	1,32	1,34	1,3	1,33	1,36	1,34	1,24	1,35	1,36	1,35	1,36	1,32
Lu	**ppm**	0,5	0,5	0,5	0,5	0,5	0,5	0,5	0,5	0,5	0,5	0,5	0,5	0,5	0,5
Mg#		42,26	44,44	—	—	—	—	—	—	—	43,32	—	—	—	—

Mg#=100*[MgO]/([MgO]+[FeOt])

FeOt=0.9*Fe2O3(t)

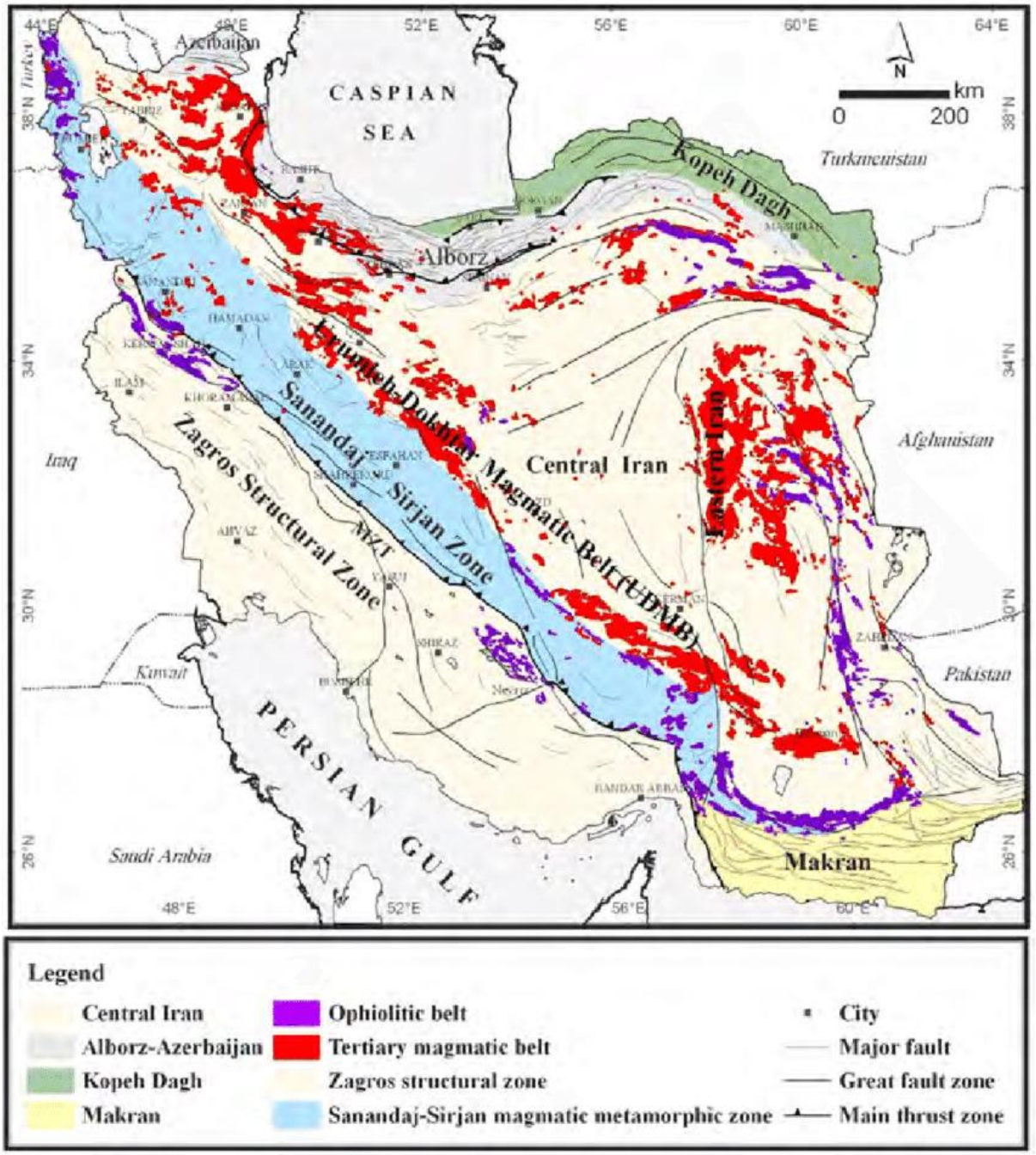

Fig. 1. Geological map of Iran (Alavi, 1994; Stöcklin and Nabavi, 1973) showing the location of sanandaj - sirjan structural zone.

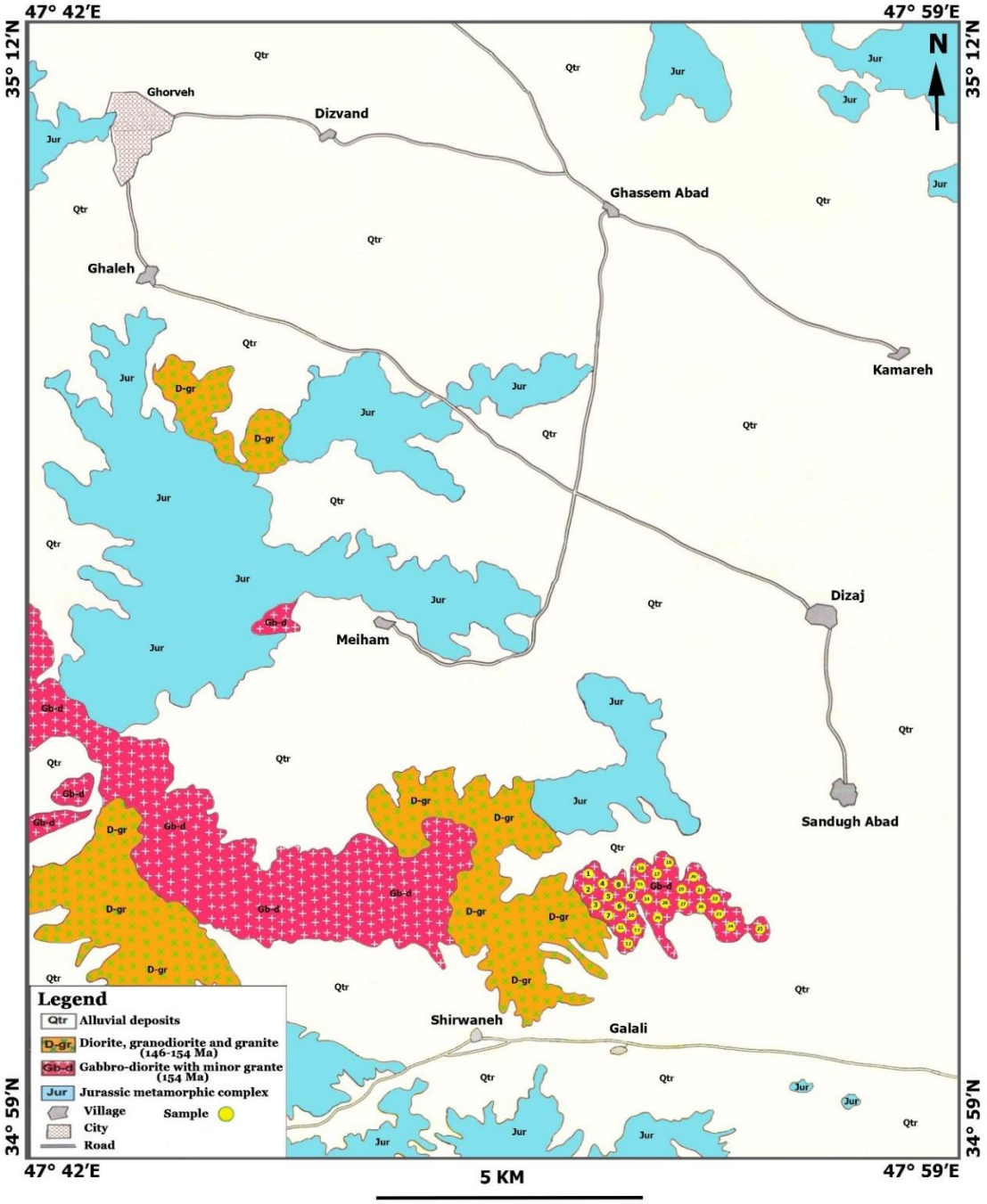

Fig. 2. Geological map of southern Ghorveh (Eshraghi et al., 1996) and sample locations. ABGs (right) and OBGs (left) in the bottom and show an almost linear structure. The main host rock is the Ghorveh-Songhor metamorphic complex of a Jurassic age. Some contact metamorphism overprints on the Jurassic metamorphic complex are due to the injection of intrusive bodies during the Late Jurassic.

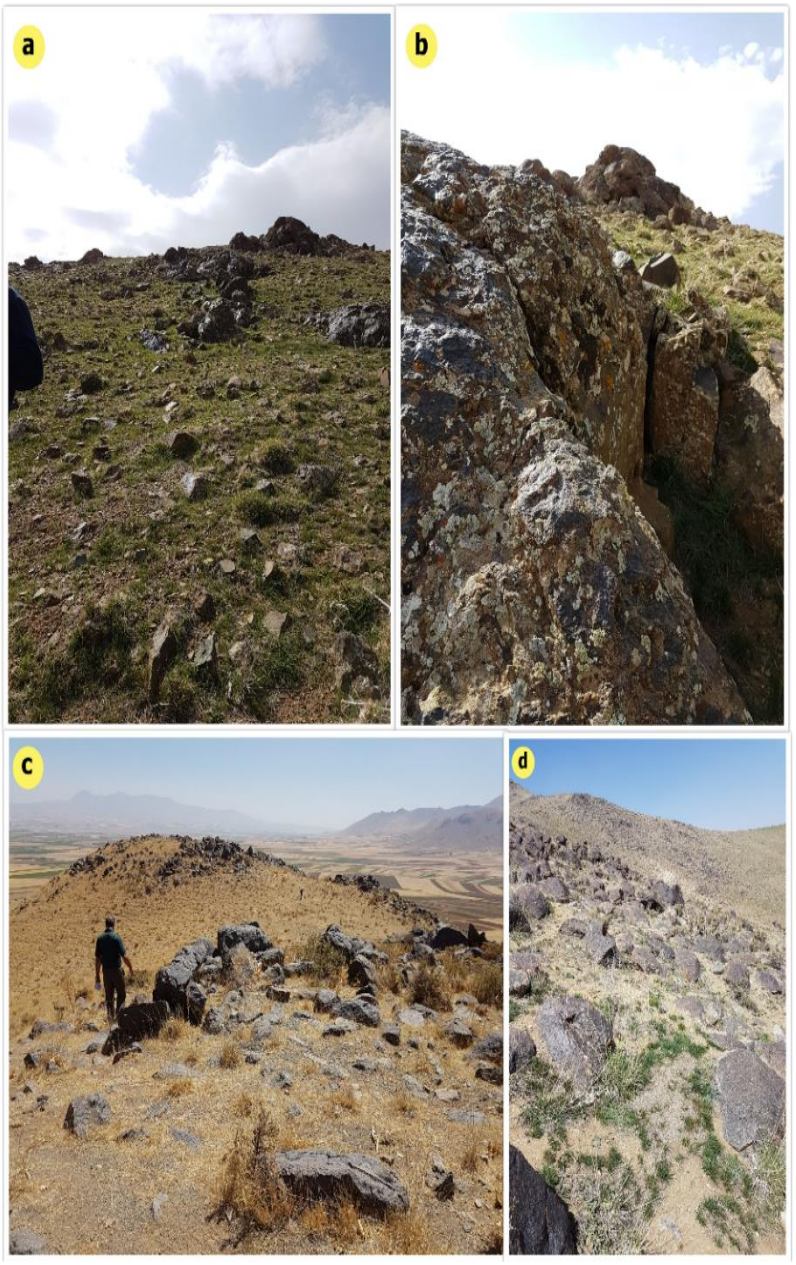

Fig. 3. (a–d) Field outcrops of ABGs in southern Ghorveh. The ABGs formed some low hills with a mound shape morphology.

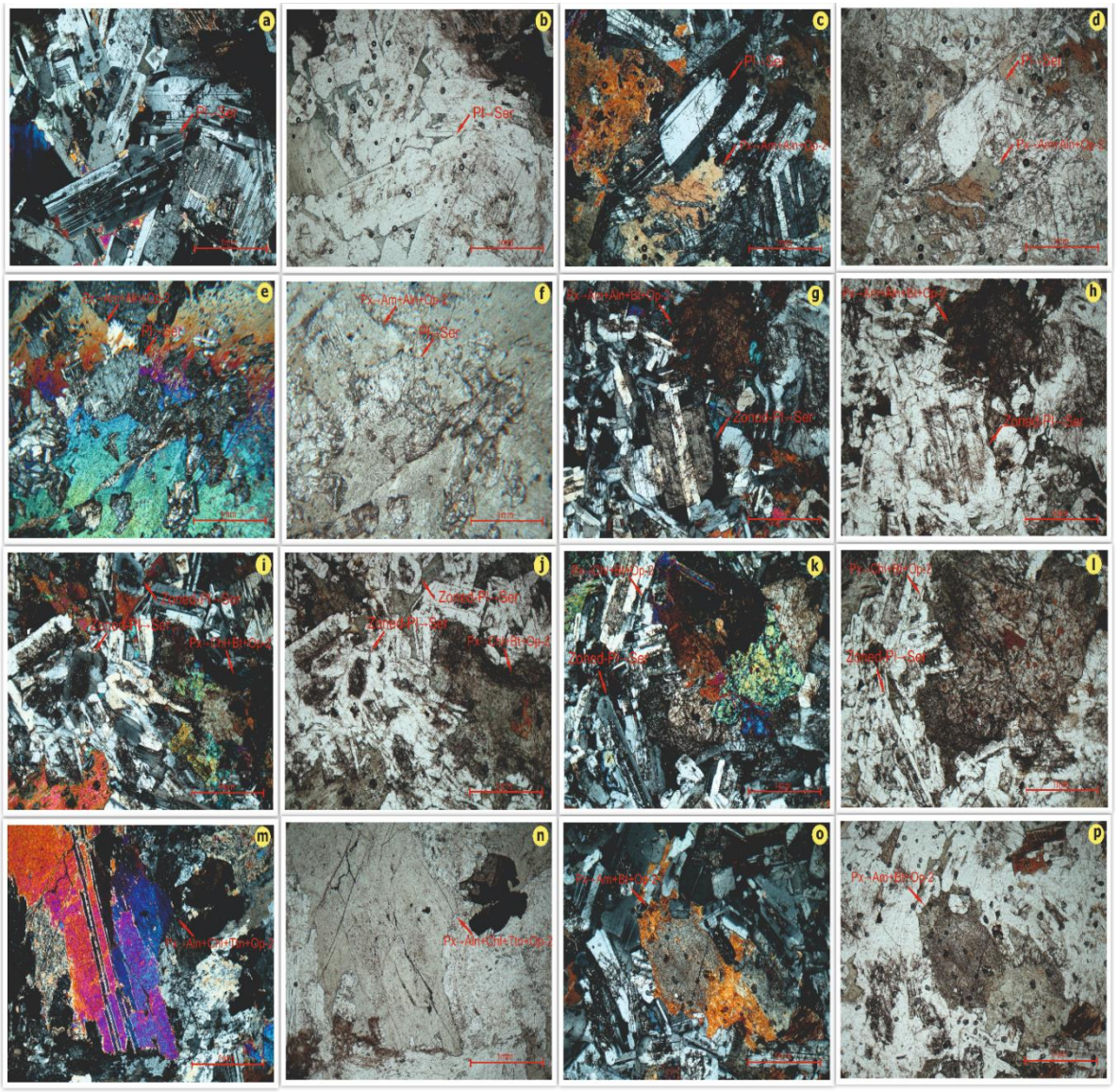

Fig. 4. Micrographic photos of ABGs in southern Ghorveh. (a–p) ABGs with granular textures as well as main minerals (e.g., plagioclase, clinopyroxene) and minor minerals (hornblende and biotite). (a–d) Different sizes plagioclases in some cases with albite-pericline and Carlsbad twins. (4e–p) Automorphic to amorphous pyroxenes (in certain cases with twining and ophitic textures), and the alteration products include amphibole, biotite, opaque minerals, and chlorite. (g–p) Plagioclases whit albite-pericline twins, Carlsbad twins, and normal zoning; and the alteration products include sericite and calcite. In plagioclases with zoning, alteration to sericite can be seen in the central parts.

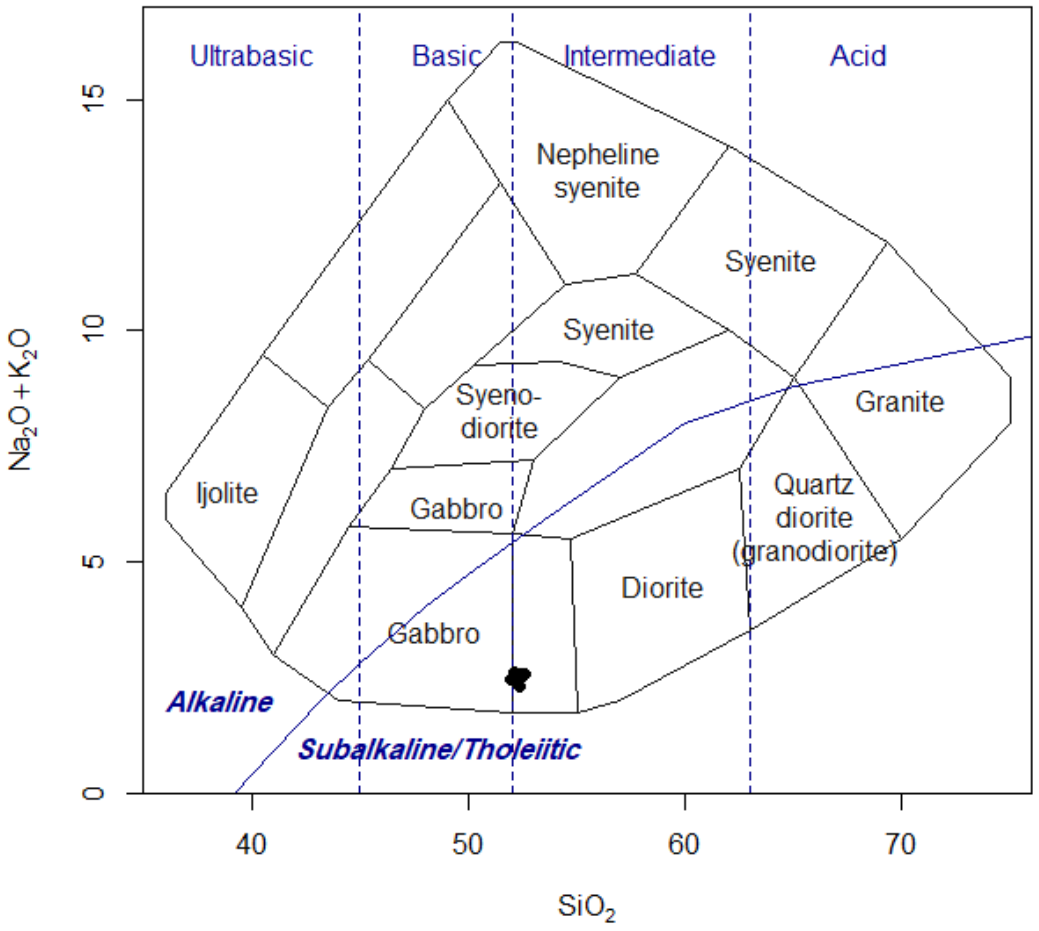

Fig. 5. Whole-rock compositions of the intrusive bodies in southern Ghorveh. In the diagram of Cox et al (1979), the samples are plotted in the gabbroic field.

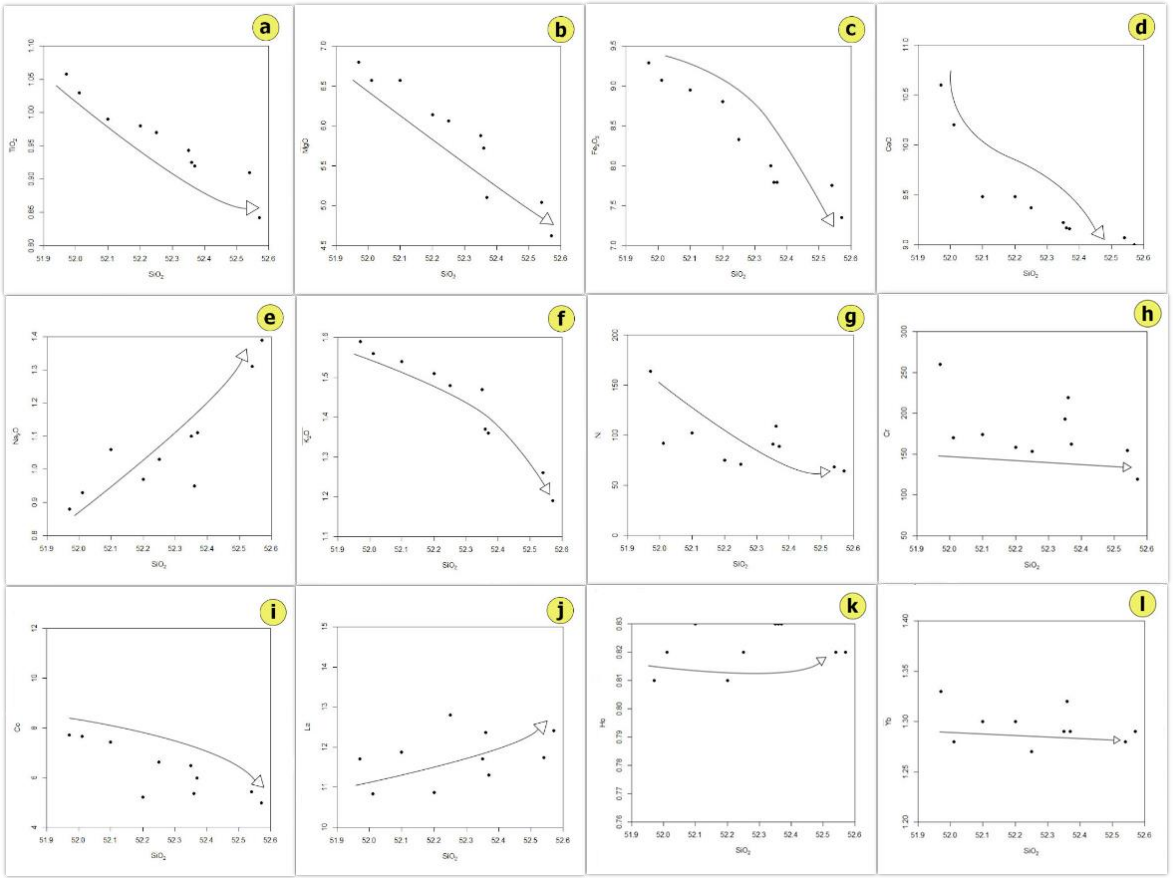

Fig. 6. Harker diagrams for major and trace elements. See the text for more details.

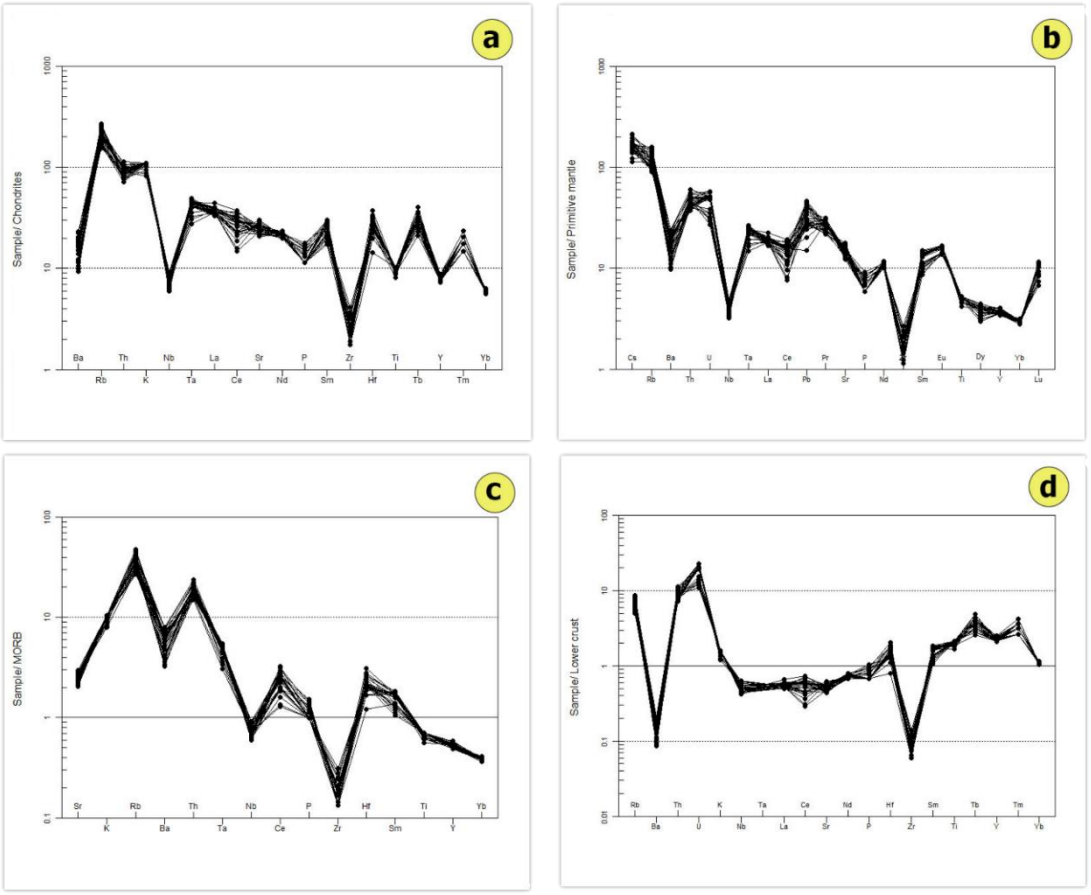

Fig. 7. Chemical compositions normalized by chondrite (Thompson, 1982), primitive mantle (McDonough and Sun, 1995), MORB (Pearce, 1983), and lower crust (Weaver and Tarney, 1984).

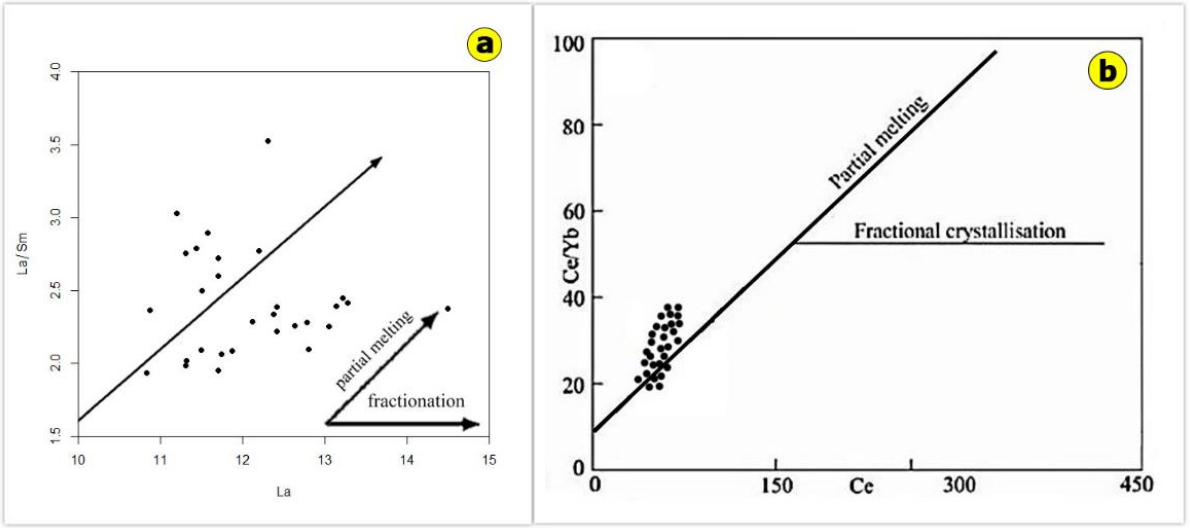

Fig. 8. (a) La/Sm vs. La diagram for the ABGs. (b) Ce/Yb versus Ce abundance shows trends compatible with varying degrees of partial melting.

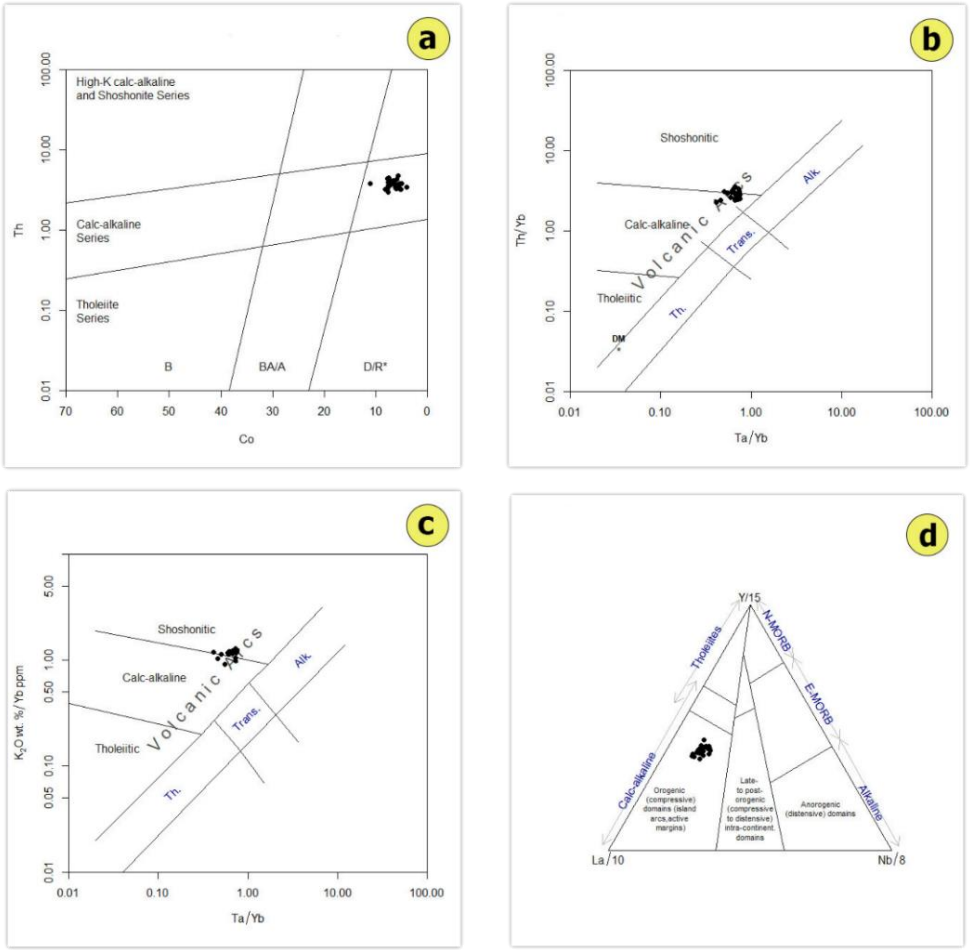

Fig. 9. Discrimination diagrams for the tectonic setting of the Jurassic intrusive bodies in southern Ghorveh. Co vs. Th (Hastie et al., 2007), Ta/Yb vs. Th/Yb and Ta/Yb vs. K2O/Yb (Pearce, 1982), and La/10- Y/15 - Nb/8 (Cabanis et al., 1989), show that the ABGs group has some affinity for active margins type magmatism.

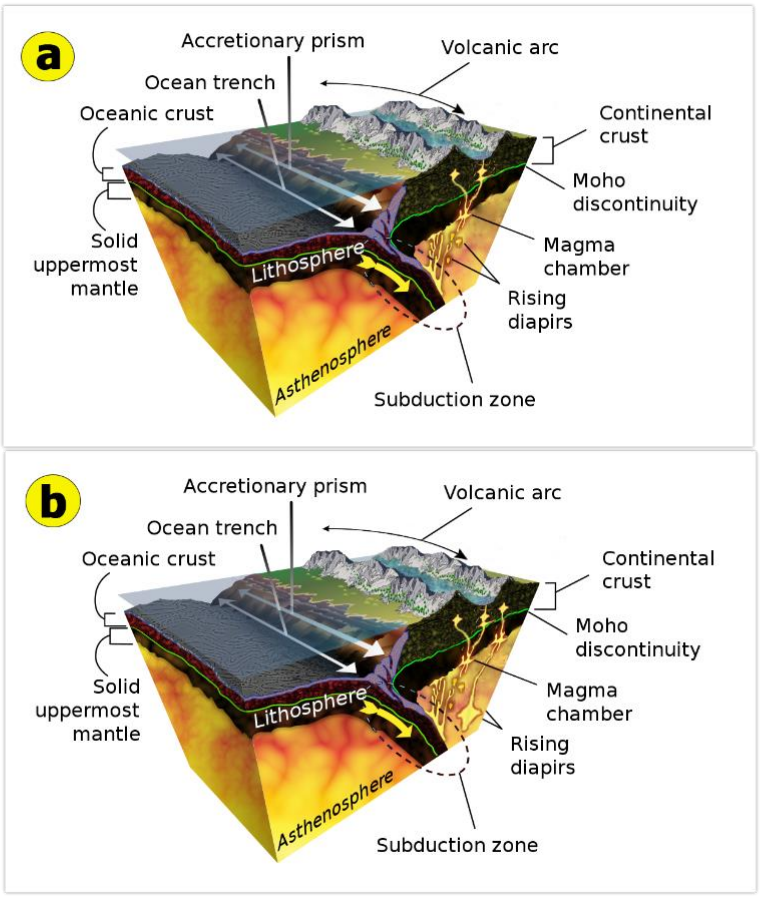

Fig. 10. A schematic model for the development of magma in intrusive bodies in southern Ghorveh. The model shows subcontinental lithospheric mantle (SCLM) as the source of mafic bodies. (a) During the first stage, calc-alkaline magma was injected into the upper continent, near the surface which causes the formation of a rift. (b) During the second stage, alkaline magma rises and goes through the assimilation-storage-homogenization process (ASH) and was injected into the upper continent, near the surface to form alkaline gabbroic bodies (OGRs) in the region (The image modified and used from Wikimedia Commons by K. D. Schroeder, CC-BY-SA 4.0. The original file is available as Subduction-en.svg).